PHOTONICS Research

Experimental evaluation of continuous and pixelated dispersive optical phased arrays for 2D beam steering

Mennatallah Kandil,[1,2,3] Mathias Prost,[1] Jon Kjellman,[1] Wim Bogaerts,[2,4] and Marcus Dahlem[1,5]

[1]IMEC, 3001 Leuven, Belgium
[2]Photonics Research Group, Ghent University - imec, 9052 Gent, Belgium
[3]e-mail: menna.kandil@imec.be
[4]e-mail: wim.bogaerts@ugent.be
[5]e-mail: marcus.dahlem@imec.be

Received 11 November 2024; revised 5 March 2025; accepted 10 March 2025; posted 10 March 2025 (Doc. ID 546057); published 30 April 2025

Dispersive optical phased arrays (DOPAs) offer a method for fast 2D beam scanning for solid-state LiDAR with a pure passive operation, and therefore low control complexity and low power consumption. However, in terms of scalability, state-of-the-art DOPAs do not easily achieve a balanced performance over the specifications of long-range LiDAR, including the number of pixels (resolvable points) and beam quality. Here, we experimentally demonstrate the pixelated DOPA concept, which overcomes the scaling challenges of classical (continuous) DOPAs by introducing a new design degree of freedom: the discretization of the optical delay lines distribution network into blocks. We also present the first demonstration of the unbalanced splitter tree architecture for the DOPA distribution network, incorporated in both the continuous DOPA and the pixelated DOPA variations. The small-scale demonstration circuits can scan over a field of view of 15° × 7.2°, where the continuous DOPA provides 16 × 25 pixels, while the pixelated DOPA provides 4 × 25 pixels, for a 1500 to 1600 nm wavelength sweep. The pixelated DOPA exhibits a side lobe suppression ratio with a median of 7.6 dB, which is higher than that of the continuous version, with a median of 3.6 dB. In addition, the ratio of the main beam to the background radiation pattern is 11 dB (median value) for the pixelated DOPA, while for the continuous DOPA, it is 9.5 dB. This is an indication of a higher beam quality and lower phase errors in the pixelated DOPA. The degree of discretization, combined with other design parameters, will potentially enable better control over the beam quality, while setting practical values for the number of pixels for large-scale DOPAs.

https://doi.org/10.1364/PRJ.546057

1. INTRODUCTION

The automotive industry has driven the research in long-range light detection and ranging (LiDAR) engines based on solid-state beam scanning, as part of a "sensor fusion" process [1]. The goal of a LiDAR system is to construct a 3D point cloud of the surrounding environment by combining two functions: beam steering and ranging. The beam steering requires sending a narrow beam to specific directions, while the ranging determines the distance of any target in the beam path through the time elapsed between the beam emission and the arrival of the back-scattered light [2]. Solid-state 2D beam steering can be performed using optical phased arrays (OPAs), where an array of optical antennas shapes and directs the beam to a certain far-field direction based on the phase delay of the light signal fed to each antenna [3]. A possible OPA implementation is to place the antennas in a 2D periodic [4] or sparse [5–7] array and control the phase of the input signal using phase shifters in the light distribution network. Such fully active tuning is challenging in terms of the circuit density, the control complexity of the individual phase tuners, and the high power consumption (in the case of thermal phase shifters).

In order to reduce the number of phase shifters, 2D beam steering can also be implemented with a 1D array of long waveguide grating-based antennas; the beam is scanned in one direction by tuning the phase shifters of the individual antennas, while a tunable laser is used to scan the beam in the other direction (as a result of the wavelength-dependent emission angle of the waveguide gratings) [8–12]. However, the complexity of the phase control can be entirely eliminated by using a single

passive control variable: the wavelength of the tunable laser. In this fully passive approach, differential delay lines are incorporated into the light distribution network instead of the active phase shifters [13–17], where the phase delay of each input light signal is now a function of the laser wavelength. Such a dispersive optical phased array (DOPA) is in essence an arrayed waveguide grating (AWG), whereas instead of imaging on an output star coupler into the waveguide modes, light radiates off-chip into the far field, using grating-based antennas. As opposed to electronically controlled OPAs, DOPAs can have faster scan rates (limited only by the scanning rate of the laser wavelength), lower control complexity (only a single control variable, i.e., the laser wavelength), and lower power consumption (the phased array is passive).

Scaling these classical DOPAs to aperture sizes large enough for projecting the light beam over a long distance with high angular resolution, is challenging due to the DOPA architecture itself, namely the delay lines feeding the antennas. Increasing the number of antennas requires adding progressively longer delay lines in the light distribution network, which in turn increases the circuit footprint and insertion loss. In addition, the inevitable accumulation of phase errors along these long waveguides [18] causes the deterioration of the beam quality. In other words, the challenge of control complexity (in the active approach) is now replaced by the challenge of the excessively large passive circuit design and high-quality fabrication (in the passive approach).

In this paper, we present the first experimental demonstration of the pixelated dispersive optical phased array concept as a solution to the bottleneck of the delay line network scaling. In addition, we conduct a comprehensive evaluation of its performance with respect to a corresponding baseline classical DOPA. Both devices use an unbalanced splitter tree architecture for the light distribution network, which is, to our knowledge, also a first experimental demonstration of this architecture in the literature. The pixelated DOPA is shown to be a promising implementation of the scanning engine that can achieve realistic long-range LiDAR requirements on a chip-scale level, with high beam quality.

2. PIXELATED DOPA CONCEPTS

DOPAs provide passive 2D beam scanning using a single variable, i.e., the laser wavelength, as shown in Fig. 1, which also indicates the parameters used in this section. In one direction, denoted here as the y axis, scanning is due to the dispersion of the long grating antennas. The far-field angle follows the grating equation, where the field of view $\Delta\theta_y$ is a function of the grating dispersion $\frac{d\theta_g}{d\lambda}$ and the available wavelength tuning range $\Delta\lambda$:

$$\Delta\theta_y = \frac{d\theta_g}{d\lambda} \cdot \Delta\lambda. \tag{1}$$

In the other direction, denoted here as the x axis, the grating antennas are arranged in a 1D array, fed by waveguide delay lines. The far-field angle is a function of the constant phase difference $\Delta\phi$ between each two consecutive antennas, following the phased array principle [19]. The phase difference is in turn a function of the wavelength λ, determined by the optical path length difference:

$$\Delta\phi = 2\pi \frac{\Delta L \cdot n_{\text{eff}}(\lambda)}{\lambda}, \tag{2}$$

where $n_{\text{eff}}(\lambda)$ is the effective refractive index of the delay line waveguide, and ΔL is the delay line length difference between

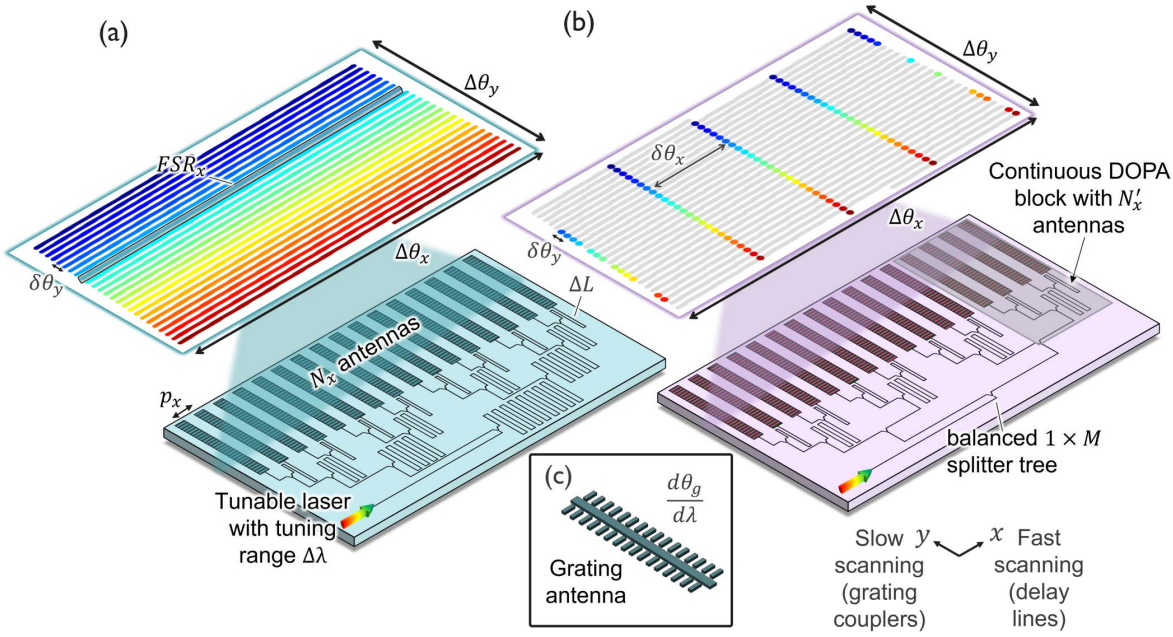

Fig. 1. Schematics of two DOPA variations implemented with an unbalanced splitter tree architecture: (a) a 16-element continuous DOPA; (b) a 16-element pixelated DOPA, where the distribution network is subdivided into four 4-element continuous DOPA blocks; and (c) schematic of the weak sidebox grating-based antenna.

each two consecutive antennas. In the x direction, the unambiguous steering field of view (FOV) $\Delta\theta_x$ is a function of the pitch between the antennas p_x [19]:

$$\Delta\theta_x \approx \arcsin\frac{\lambda}{p_x}. \tag{3}$$

Since ΔL is larger than the periodicity of the gratings, the scanning rate along the x direction (fast axis) is much faster than along the y direction (slow axis). For a specific wavelength sweep rate of the laser, a longer ΔL results in $\Delta\phi$ sweeping faster through the $[0, 2\pi]$ interval. The wavelength range required for one complete 2π phase cycle is the free spectral range along the x axis FSR_x:

$$\mathrm{FSR}_x \approx \frac{\lambda^2}{n_g \cdot \Delta L}, \tag{4}$$

where n_g is the group index of the delay line waveguide. One full scan covering the FOV along the x direction is a scan line, achieved by a wavelength range equal to FSR_x. The number of resolvable points in the y direction N_y (the number of scan lines) is then a function of FSR_x:

$$N_y = \frac{\Delta\lambda}{\mathrm{FSR}_x} = \frac{\Delta\theta_y}{\delta\theta_y}, \tag{5}$$

where $\delta\theta_y$ is the y axis sampling resolution, i.e., the angular separation between each two consecutive resolvable points in the y direction. In this DOPA variation, for each wavelength point, there is a corresponding far-field location where a narrow beam is formed. This means that a narrow beam is continuously scanned along the x axis upon scanning the laser wavelength, which is why we name this classical DOPA variation a continuous DOPA, as shown in Fig. 1(a).

Continuous DOPA implementations define the x axis far-field sampling resolution specification to be the same as the x axis beam divergence specification (see Appendix B for further explanation on the specifications of resolution and beam divergence along the x direction). The x axis far-field sampling resolution $\delta\theta_x$ is the angular separation between each two consecutive resolvable points in the x direction, and the beam divergence is the full width at half-maximum FWHM_x of the spot at the maximum range, i.e., the Rayleigh range. In other words, for a diffraction-limited DOPA, which can be achieved in a platform with low losses and low phase errors, the number of resolvable points in the x direction, N_x, is equal to the total number of antennas. Consequently, for a circuit designed to fulfill the required beam divergence for LiDAR, requiring a large number of antennas, the number of resolvable spots is orders of magnitude higher than the typical LiDAR requirement. For example, for a maximum range (Rayleigh range) of 200 m and x direction FOV of 50° [20], the required beam divergence is 0.01°. This translates to the number of antennas equaling 8192. On the other hand, the angular resolution requirement is 0.1°, translating into the number of antennas equaling 512, where the number of antennas is rounded to the next power of 2 [21]. However, the pixelated DOPA, shown in Fig. 1(b), decouples these two specifications by subdividing the light distribution network into smaller blocks. The total number of antennas N_x is now defined as $N_x = MN'_x$, where M is the number of blocks and N'_x is the number of antennas per block. The blocks are fed by a $1 \times M$ balanced splitter tree, while the aperture is kept the same as in the continuous DOPA. As a result, the phase relation between the last and the first antennas of adjacent blocks is broken, and a narrow far-field spot only exists at specific wavelengths, i.e., the operation wavelengths λ_m [22]:

$$\lambda_m = \frac{N'_x}{m} \cdot \Delta L \cdot n_{\mathrm{eff}}(\lambda). \tag{6}$$

When scanning the laser wavelength, the constructive interference condition for a narrow beam is now satisfied for discrete wavelengths, corresponding to discrete far-field locations. For this reason, we name this DOPA variation the pixelated DOPA. Here, the number of resolvable points along the x axis equals the number of antennas within a block N'_x, and the angular resolution along the x direction $\delta\theta_x$ is

$$\delta\theta_x \approx \frac{M}{N_x}.\arcsin\frac{\lambda}{p_x}. \tag{7}$$

This additional degree of freedom in the distribution network significantly reduces the total length of the delay lines, simplifying the circuit design and reducing both the optical losses and phase errors.

3. DEVICE DESIGN AND FABRICATION

In this work, we aim to experimentally demonstrate the pixelated DOPA concept and compare it one-to-one with a continuous DOPA with the same aperture design. Hence, we designed and fabricated a circuit for each variation [schematics are shown in Figs. 1(a) and 1(b)], where the two circuits have the same aperture design, differential delay line length ΔL, and distribution network choice. The center wavelength is 1550 nm with a span of 100 nm.

When defining the circuit on the schematic level, our first design parameter is the choice between Si and SiN for the

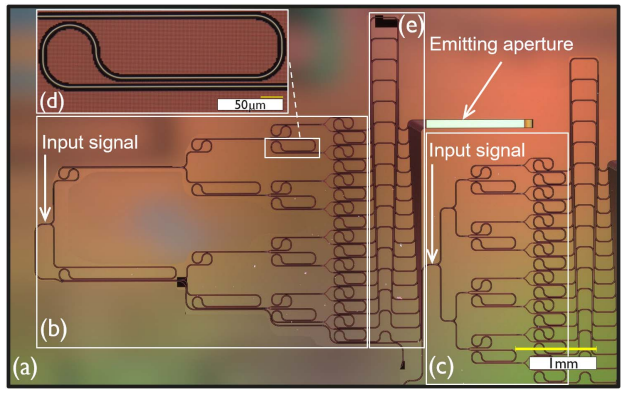

Fig. 2. Microscope image of the fabricated devices in SiN, where other non-relevant devices are blurred out: (a) full microscope image showing the circuit of the continuous DOPA and the distribution network of the pixelated DOPA; (b) distribution network of the continuous DOPA; (c) distribution network of the pixelated DOPA; (d) close-up on one of the meander-shaped delay lines; and (e) delay-maintaining fan-in routing used to match the output pitch of the distribution network and the antenna array, while not adding extra delay between the antennas.

waveguiding layer; these are the two key materials for compact photonic circuits and wafer-scale manufacturing. Si allows for more compact waveguides and bends, and allows higher group velocity index than SiN, requiring a shorter delay length ΔL for the same target number of scan lines, following Eqs. (4) and (5). On the other hand, SiN waveguides exhibit lower phase errors [23], which should result in a better beam quality in terms of diffraction-limited beam divergence and side lobe suppression ratio (SLSR), where the SLSR is the ratio between the main lobe and the highest side lobe.

The differential delay ΔL between the antennas can be introduced through different architectures, namely the AWG, demonstrated in Refs. [13,15–17]; the snake, demonstrated in Ref. [14]; and the unbalanced splitter tree. The latter was suggested in Ref. [22] but has not yet been demonstrated experimentally. As discussed in Ref. [22], the unbalanced splitter tree strikes a balance between an arrayed waveguide grating with fully independent waveguides, and a snake bus waveguide with controlled power taps, which does not scale well because of the difficulty in designing power taps with a very small but controlled coupling fraction. In addition, it has an intermediate performance sitting between the AWG and the snake architectures in terms of insertion loss and footprint [21]. In this work, we opted for the unbalanced splitter tree architecture fabricated on an LPCVD SiN stack in IMEC's 200 mm pilot line. This platform has low propagation loss and low phase errors [24]. However, this results in a relatively large bend radius which increases the size of the circuit. In addition, our focus here is on the circuit demonstration, while the individual building blocks can be further optimized. We therefore use simple and proven components to build the circuits where possible.

The emitting aperture consists of a 16-element antenna array, with a pitch of 6 μm to circumvent any possible evanescent coupling between the antennas. This gives a theoretical x axis FOV $\Delta\theta_x$ of 15°, and a beam divergence FWHM$_x$ of 0.87° at 0° emission angle [19]. The optical antenna is implemented using weak sidebox gratings, as shown in Fig. 1(c), with a period of 1 μm. The grating antenna is designed to have a strength of ≈17 dB/mm, resulting in an effective antenna length below 1 mm. The simulated scan rate of the grating is ≈0.07 deg/nm, resulting in a y axis FOV of ≈7° for a 100 nm wavelength range. However, the metrics associated with the grating antenna design can differ after fabrication, since the grating is not a proven component provided by the platform. For this demonstration, we aimed to populate the y axis FOV with 25 scan lines for the selected 100 nm wavelength range. We calculated the waveguide group velocity index n_g to be 2.0, based on the SiN waveguide dimensions and the material refractive indices, through mode simulations. The differential delay line length ΔL is then 300 μm, calculated from Eqs. (4) and (5), around a center wavelength of 1550 nm.

A microscope image of the fabricated devices is shown in Fig. 2. On the circuit layout level, the unbalanced splitter tree architecture requires that only half of the arms in each splitter stage have a delay line. We used meander-shaped delay lines with bend radius of 60 μm, as shown in Fig. 2(d). Here, the delay lines are added at the south output arm of the splitter at each level of the splitter tree. However, we also added meanders to the north output arm to provide balance in the number of bends, as shown in Fig. 2(b). Splitters based on 1 × 2 MMIs, with a footprint of 62.5 μm × 5 μm including the tapers, are used. Due to the footprint of the meanders, the output pitch of the distribution network does not match the desired array pitch p_x. A fan-in routing is used to match the pitches while not adding extra delay between the antennas (delay-maintaining fan-in), as shown in Fig. 2(e). Note that for this circuit, we separated these design concerns in different sections of the circuit, resulting in a larger-than-necessary footprint.

For the pixelated DOPA, the same design choices are followed in order to compare the two variations, except for the distribution network which is subdivided into four blocks fed by a balanced splitter tree, as shown in Fig. 2(c). Thereby, the pixelated DOPA is expected to have approximately four pixels per scan line, matching the number of antennas N'_x in a single block. Moving from the continuous DOPA to the pixelated DOPA, the number of splitting levels of the unbalanced tree is reduced from four to two, and the longest delay line length path is reduced from 4.5 to 0.9 mm, respectively, which should improve the beam quality due to lower phase errors.

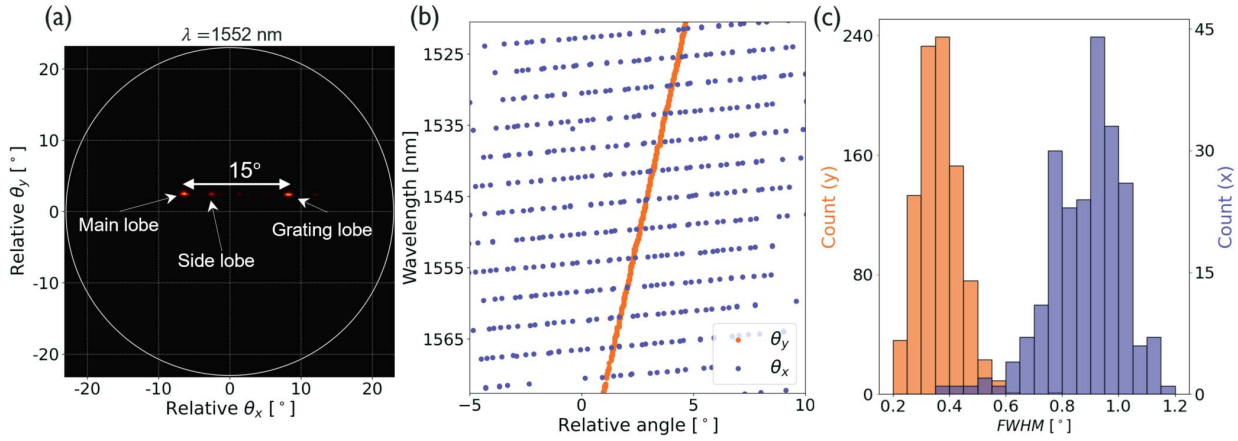

Fig. 3. Measurement results of the fabricated continuous DOPA: (a) far-field image at 1552 nm, showing the main lobe and a grating lobe separation of ≈15°; (b) scan rates along the x and y directions of ≈3.66 and ≈0.072 deg/nm, respectively; and (c) histogram of the FWHM measurements along the x direction with a median of 0.92°, and the y direction with a median of 0.36°.

4. RESULTS AND DISCUSSION

We perform a broadband measurement of the continuous DOPA far field as proof of the unbalanced splitter tree architecture and as a baseline for the pixelated DOPA. We extract the FOV, scan rate, and FWHM, where the far-field images are acquired through a Fourier imaging setup. The images are processed to locate the main lobe, grating lobes, and side lobes pixels through a peak detection algorithm.

For the x axis, the FOV $\Delta\theta_x$ is 15° around 1550 nm, while the scan rate $\frac{d\theta_x}{d\lambda}$ is ≈3.66 deg/nm, as shown in Figs. 3(a) and 3(b). As a result, the wavelength range required to sweep over one scan line FSR_x equals $\Delta\theta_x/(\frac{d\theta_x}{d\lambda}) \approx 4.1$ nm (see Visualization 1), corresponding to ≈24.5 scan lines for a 100 nm wavelength range, following Eq. (5). The beam divergence is a function of the wavelength and the emission angle [19] and varies slightly with the introduction of phase errors [25]. Since it is difficult to disentangle these dependencies, we report the histogram of the beam divergence for the x axis FWHM_x based on 225 data points, as shown in Fig. 3(c). The median FWHM_x is 0.92°, so it follows that the far-field sampling resolution $\delta\theta_x$ is ≈0.92°. This indicates that we have 16 fully resolvable points per scan line, and the wavelength step required to move from one fully resolvable point to the next along a scan line is ≈240.4 pm. Along the y axis, the scan rate $\frac{d\theta_y}{d\lambda}$ is ≈0.072 deg/nm [Fig. 3(b)], which means that the FOV $\Delta\theta_y$ is 7.2° for the 100 nm tuning range. Based on the number of scan lines and the FOV, the far-field sampling along the y axis $\delta\theta_y$ is $\approx 7.2°/24.5 = 0.29°$. The histogram of the beam divergence along the y axis FWHM_y, based on 910 data points, is shown in Fig. 3(c), where the median FWHM_y is 0.36°, meaning that the effective antenna length is ≈225 μm, which deviates from the design. The deviation is expected because of the fabrication variations that are more pronounced with the small geometric perturbations required for weak gratings [26] and because of the phase errors along the grating antenna [27]. On the other hand, the number of pixels and FOV along the x and y directions match the design specifications. Beam steering results over a 100 nm wavelength range are shown in Fig. 4.

In order to compare both DOPA variations in terms of the phase errors, we investigate the background of side lobes between the main lobe and the grating lobes. This is especially important because these phase errors, resulting from the geometry variations, are not compensated after the fabrication of such passive devices. Phase and amplitude errors cause power to be redistributed between the main lobe, grating lobes, and the side lobes. The SLSR, that is the ratio between the main lobe and the highest side lobe, has been conventionally used as an indicator of the phase errors of active and passive OPAs. However, looking only at the highest side lobe can give a skewed picture of the phase errors in the OPA, as it ignores the light directed to the background, i.e., to all the other angles outside the main lobe. The background can be indicated by the crosstalk suppression, which we calculate by excluding the main

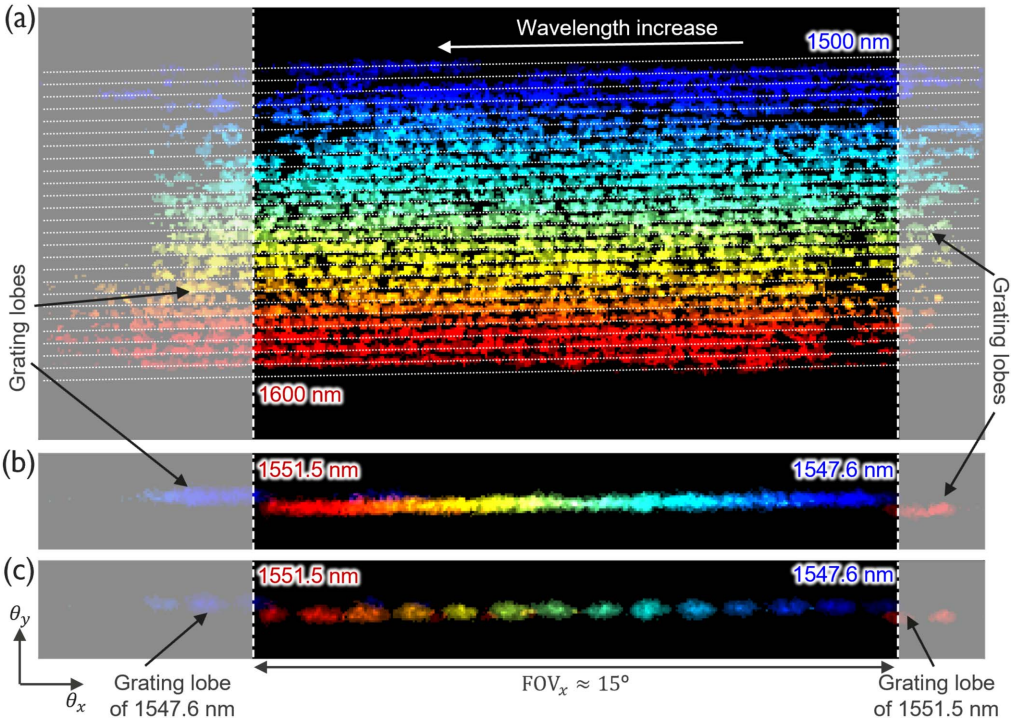

Fig. 4. 2D beam steering results of the continuous DOPA. (a) Composite image of the far-field images of wavelength scan from 1500 to 1600 nm with a step of 0.1 nm (see Visualization 2), where the FOV is 15° × 7.2°. For each image forming the composite, only the pixels with value higher than a certain threshold are shown to visually differentiate the scan lines. (b) A single scan line with the same wavelength step as (a), i.e., 0.1 nm. However, a lower threshold than in (a) is used and a visually continuous scan line can be observed, since the wavelength step here is less than the step required to move from one fully resolvable point to the next, i.e., 0.24 nm. (c) A single scan line with the same threshold as in (b) and a wavelength step of 0.3 nm.

lobe and grating lobe pixels and then taking the 90th percentile of all other pixels (see Appendix C for further details on this method).

Considering FMCW ranging, the redistribution of light away from the main lobe due to phase errors reduces the useful signal level. This redistribution is well characterized by the crosstalk suppression. Additionally, prominent spikes in the side lobes can, from the receiver's point of view, produce beat signals that are indistinguishable from the main lobe beat signal, resulting in erroneous or ambiguous ranging. In the worst-case scenario, this erroneous beat signal might dominate the main lobe beat signal if it is reflected from a target closer than the target along the path of the main lobe. Such spike events in the side lobes are well described by the SLSR. Therefore, we propose that in addition to using SLSR when evaluating OPAs, crosstalk suppression should also be used as an indicator for the level of phase errors and its impact. We extract the SLSR using a method similar to Ref. [10]. We calculate the SLSR values of the continuous DOPA at 790 wavelength points. The median of these points is 3.6 dB, and the histogram of the measurements is shown in Fig. 5(a). The crosstalk suppression of the continuous DOPA has a median of 9.5 dB, and the histogram of the measurements is shown in Fig. 5(a).

To demonstrate the beam steering of the pixelated DOPA, we first pinpoint the wavelengths at which the constructive interference occurs, i.e., the operation wavelengths. We extract the SLSR at different wavelengths, and it can be observed that the operation wavelengths are local maxima for the SLSR, as shown in Fig. 5(e). After identifying those wavelengths, we show the beam steering results of the far-field pixels of the pixelated DOPA in Fig. 6(a). The constructive interference wavelengths are separated by ≈1 nm, denoting that the wavelength step required to move from one pixel to the next along a scan line is ≈1 nm (see Visualization 1). The FOV along the x direction $\Delta\theta_x$ is 15° around 1550 nm, while the scan rate $\frac{d\theta_x}{d\lambda}$ is ≈3.66 deg/nm and the median FWHM_x is 0.97°, as shown in Figs. 7(a)–7(c). Along the y axis, the scan rate $\frac{d\theta_y}{d\lambda}$ is ≈0.072 deg/nm, which means that the FOV $\Delta\theta_y$ is 7.2° for the 100 nm tuning range, and the median FWHM_y is 0.36°, as shown in Figs. 7(b) and 7(c). The far-field sampling along the x direction $\delta\theta_x$ is then ≈3.66°, corresponding to 4 pixels per scan line, as shown in Fig. 6(b), which matches the number of antennas per block N_x'. We calculate the SLSR and crosstalk suppression of the pixelated DOPA at the constructive interference (operation) wavelengths, at 70

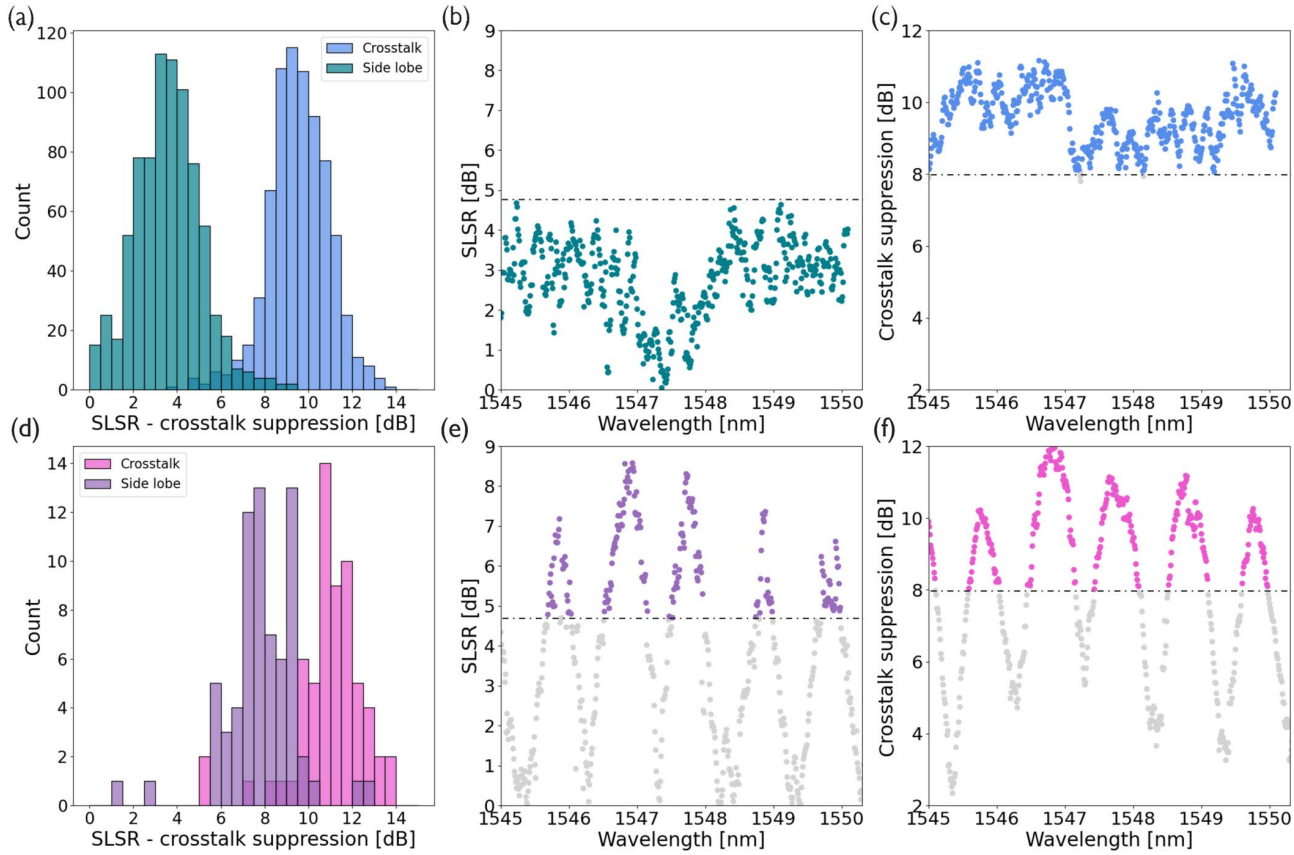

Fig. 5. Side lobe suppression ratio (SLSR) and crosstalk suppression measurement results of the DOPA devices. (a) Histogram of the SLSR and crosstalk suppression of the continuous DOPA corresponding to a wavelength range of 1500 to 1600 nm, with median SLSR value of 3.6 dB and median crosstalk suppression value of 9.5 dB. (b), (c) SLSR and crosstalk suppression, respectively, of the continuous DOPA versus the wavelengths. (d) Histogram of the SLSR and crosstalk level of the pixelated DOPA at the constructive interference wavelengths, with a median SLSR value of 7.6 dB and a median crosstalk suppression value of 11 dB. (e), (f) SLSR and crosstalk suppression, respectively, of the pixelated DOPA versus the wavelengths, showing the local maxima of the SLSR corresponding to the constructive interference wavelengths.

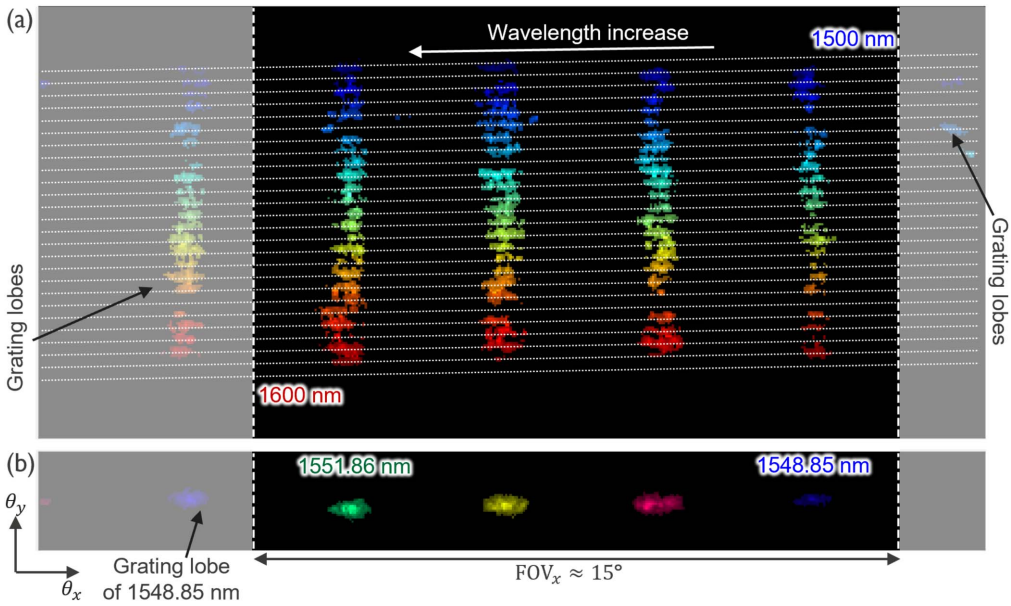

Fig. 6. 2D beam steering results of the pixelated DOPA. (a) Composite of the far-field images of the wavelength scan from 1500 to 1600 nm at the constructive interference wavelengths (see Visualization 3). For each image forming the composite, only the pixels with value higher than a certain threshold are shown to visually differentiate the scan lines. (b) A single scan line showing four pixels per scan line. However, a lower threshold than in (a) is used to show the spot clearly.

and 63 wavelength points, respectively. The median of the SLSR is 7.6 dB, while the median of the crosstalk level is 11 dB. The histogram of the measurements is shown in Fig. 5(d).

One of the key advantages of the pixelated DOPA can be understood in view of the trade-off between the number of resolvable points along the y direction and the phase errors of the circuit. These phase errors can be traced in DOPAs, due to their passive operation, in the form of a degraded SLSR from the expected theoretical values [14,15,17] (see Appendix A for further elaboration on the literature of DOPAs). The fabricated DOPAs always exhibit worse SLSR than the theoretical value due to the effective refractive index variation along the waveguides introduced by the process variations. Such variations result in deviations in the optical path lengths within the distribution network, which subsequently introduce errors in the input phase to the antennas of the optical phased arrays, deteriorating the far-field beam quality. On the other hand, to achieve higher y axis resolution $\delta\theta_y$ with a specific technology implementation and a given laser wavelength range, it is necessary to increase the differential delay length ΔL, following Eq. (4). A well-designed continuous DOPA should balance these performance metrics. On the other hand, the pixelated DOPA relaxes this trade-off by introducing a new design parameter, that is, the number of resolvable points along the x direction, through the discretization of the distribution network into blocks, i.e., pixelation of the far field. In this work, the SLSR of the pixelated DOPA exceeds that of the continuous DOPA at the operation wavelengths where a collimated beam exists. Furthermore, the pixelated DOPA remains functionally superior to the continuous DOPA, in terms of the SLSR, within a considerable wavelength range around these operation wavelengths, as shown in Figs. 5(b) and 5(e). As for the crosstalk suppression, the pixelated DOPA has better performance than the continuous DOPA at the operation wavelengths and a similar performance within a considerable wavelength range around these operation wavelengths, as shown in Figs. 5(c) and 5(f).

The pixelated DOPA adjusts the design space of the scanning engine. For a specific group velocity index of the distribution network waveguides, the requirement of the number of pixels in the y axis (the total number of scan lines) determines the shortest delay line length ΔL for both the pixelated DOPA and the continuous DOPA. For a specific architecture choice and in the case of the continuous DOPA, the total number of antennas required to achieve the beam divergence in the x axis determines the number of resolvable pixels per scan line in the x axis, and hence the length of the longest delay line. However, in the case of the pixelated DOPA, the requirement of the number of pixels per scan line in the x axis determines the degree of discretization, i.e., the number of antennas per block, regardless of the beam divergence requirement. Hence, the degree of discretization determines the length of the longest delay line. The pixelated DOPA can thereby satisfy the requirement of the number of pixels along the y direction and achieve high beam quality by setting the number of pixels along the x direction to more practical values, and hence reducing the total length of the delay lines.

Figure 6 shows that there are large scanning blind spots along the x direction. This is due to the small scale of this proof-of-concept demonstration, where the pixelation of the far field is very strong, resulting in 3.66° resolution along the x direction. Comparing Figs. 5(b) and 5(e), the wavelength range around the operation wavelengths for which the pixelated DOPA has higher SLSR than the continuous one amounts to

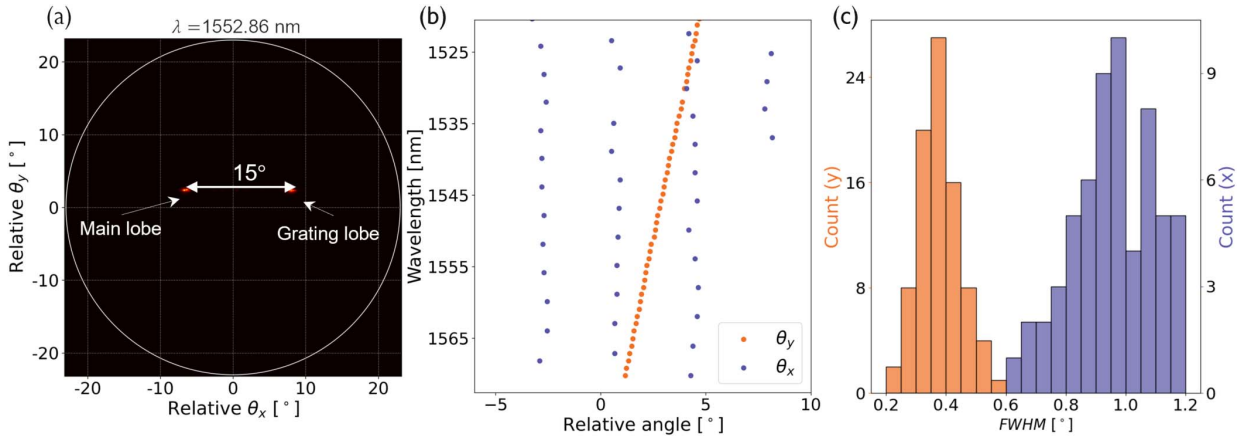

Fig. 7. Measurement results of the fabricated pixelated DOPA: (a) far-field image at 1552.86 nm, showing the main lobe and a grating lobe separation of ≈15°; (b) scan rates along the x and y directions of ≈3.66 and ≈0.072 deg/nm, respectively; and (c) histogram of the FWHM measurements along the x direction with a median of 0.97°, and the y direction with a median of 0.36°.

Table 1. Comparison of DOPA Architectures

Method	Ref. [13]	Ref. [14]	Ref. [15]	Ref. [16]	Ref. [17]	CDOPA	PDOPA
Architecture	AWG	Snake	AWG	AWG	AWG	Unbalanced tree	Unbalanced tree
Platform	Si	Si	SiN	SiN	Si	SiN	SiN
N_x	16	32	39	128	128	16	16
p_x [μm]	2	16	6	4	2.07	6	6
ΔL [μm]	87.7	>1600	65.4	54	20	300	300
$\delta\theta_x$ [°]	3.5–4	0.2	0.36	0.16	0.233	0.92	3.66
$\delta\theta_y$ [°]	1.14	0.059	1.4	1.7	3.47	0.29	0.29
$\Delta\theta_x$ [°]	50	5.5	15	22.9	43.9	15	15
FWHM_x [°]	4	0.2	0.36	0.16	0.233	0.92 (median)	0.97 (median)
FWHM_y [°]	3.5–4	0.11	0.175	0.13	0.05	0.36 (median)	0.36 (median)
SLSR [dB]	—	3 @ 1550 nm	10–30	12.61	4.16	3.6 (median)	7.6 (median)

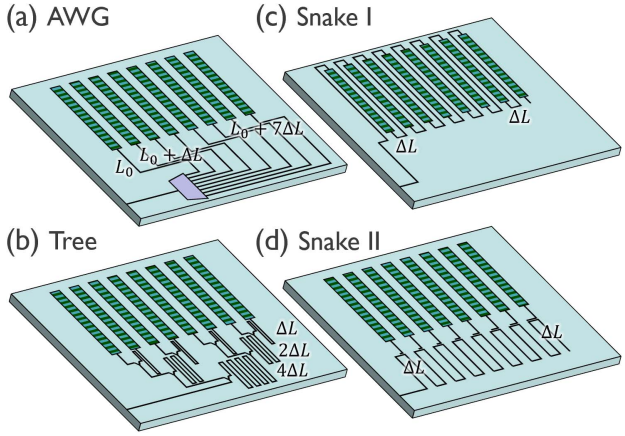

Fig. 8. Different DOPA architectures. (a) The AWG which consists of a parallel bundle of waveguides with incremental increase in the waveguide length by ΔL. (b) The unbalanced splitter tree which is presented in this work. The delay is added to one arm of each splitter. In each stage m, the delay added to the splitter arm is $2^m\Delta L$. (c) The snake using the implementation of Ref. [14], where the delay is introduced by the grating antennas and the "flyback" waveguides. (d) An alternative implementation of the snake, presented in Ref. [22], where light is distributed via a bus waveguide. The light is tapped off to the grating antennas at fixed distances ΔL.

approximately 0.4 nm, which translates into a bandwidth of 50 GHz. On the other hand, due to the large differential delay used, the resolution of 0.29° along the y direction is very close to the 0.1° of LiDAR requirement, where the blind spots are very small. A clever design should balance the degree of discretization and the differential delay length to fulfill the number of pixels requirement while maintaining high beam quality.

In a scaled-up implementation, both the number of pixels in the x and y directions would rise. And the wavelength range around the operation wavelengths for which the pixelated DOPA maintains high SLSR would be around 8 to 24 pm, which translates into a bandwidth of 1 to 3 GHz around the operation wavelengths. This bandwidth is specifically important for swept source FMCW LiDAR, where the beam steering and ranging are done with the same wavelength variable [28]. To perform the FMCW ranging, the tunable laser needs to sweep over a bandwidth of a few GHz, while maintaining its position on the same pixel with a good beam quality. However, scaling implies the accumulation of phase errors even with the pixelated approach. Without further improvement in the process control to reduce geometry variations, phase error correction would be necessary either through adding phase tuners at an intermediate level of the tree or by phase trimming [29].

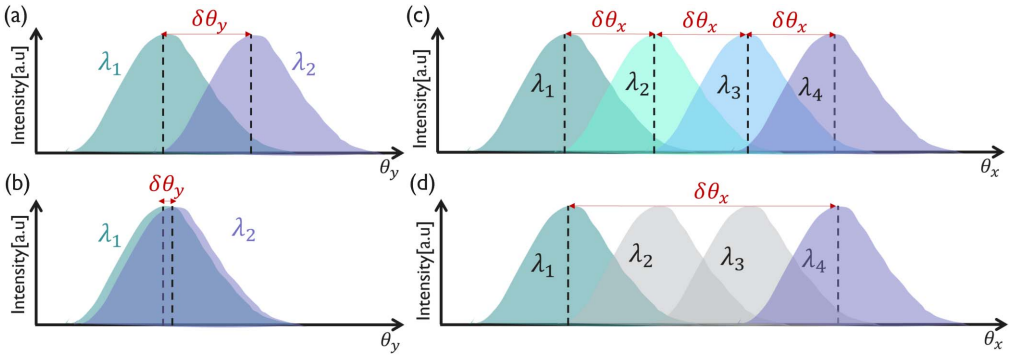

Fig. 9. Angular resolution considerations. (a) The angular resolution along the y axis $\delta\theta_y$ is defined by the differential delay length. The number of resolvable points is then $N_y = \frac{\Delta\theta_y}{\delta\theta_y}$, provided that the spot size along y is smaller than or equal to $\delta\theta_y$. (b) $\mathrm{FWHM}_y > \delta\theta_y$, and hence, the number of resolvable points along y is limited by the spot size. In this case, ΔL is larger than necessary and only contributing to extra phase errors. (c) The angular resolution in the x direction $\delta\theta_x$ of the continuous DOPA is considered equivalent to the angular separation between two fully resolvable points along the x direction, i.e., the beam divergence. (d) The angular resolution along the x direction $\delta\theta_x$ of the pixelated DOPA depends on the number of antennas per block and is independent of the beam divergence.

The input of the pixelated DOPA is compatible with star couplers, where the $1 \times M$ splitter tree in our demonstration would be replaced by an $N \times M$ star coupler, allowing multiplexing. Tunable lasers with different wavelength bands can be connected to different input ports. Each tunable laser can cover a band that is a subsection of the full wavelength tuning range, enabling wavelength multiplexing for fast frame rates [28]. The choice of the wavelength bands and the position of the star coupler input ports can be designed such that for a single wavelength, two or more far-field locations are addressed simultaneously, allowing for spatial multiplexing, similar to Ref. [15]. Such multiplexing schemes are compatible with current hybrid 3D integration technologies using flip chip bonding [30] or transfer printing [31]. The star coupler also allows for a Gaussian power distribution over the blocks to improve the beam quality [32].

The FOV along the x direction can be improved by reducing the DOPA pitch and designing the antenna such that the antenna's element factor suppresses any remaining grating lobes. Furthermore, the scanning in the y direction can be improved through the optimization of the antenna design. Long antennas can be achieved by stepping aside from the traditional weak gratings to new antenna concepts like the leaky fin antenna, proposed in Ref. [26]. In terms of the circuit layout, further optimization can be done for a compact circuit, for example, by designing compact MMIs, adiabatic bends [33], placing the meanders more compactly, and using the delay of the fan-in waveguides as part of the circuit differential delay.

5. CONCLUSION

In this paper, we have demonstrated the 2D beam steering of the continuous and pixelated variations of the dispersive optical phased arrays, in a 16-channel unbalanced splitter tree architecture. For a wavelength steering range of 1500 to 1600 nm, the devices have an FOV of $15° \times 7.2°$, where the continuous DOPA steers over 16×25 pixels, while the pixelated DOPA steers over 4×25 pixels. The pixelated DOPA shows better performance in terms of the side lobe suppression ratio and the crosstalk suppression at these pixels. The pixelated DOPA can therefore be a solution to the scaling bottleneck of dispersive optical phased arrays, paving the way for large-scale low-complexity long-range solid-state LiDAR.

APPENDIX A: COMPARISON OF DOPA ARCHITECTURES

We compare the performance of our implementations of a DOPA, in particular the continuous DOPA (CDOPA) and the pixelated DOPA (PDOPA), to the implementations of DOPA published in the literature for 2D beam steering in Table 1. The different design choices make a one-to-one comparison for some metrics difficult; however, we can still extrapolate to estimate the scaling of the DOPA implementations. One of the main implementation choices is in the distribution network. In a DOPA, we feed the array of antennas with delay lines with a linear increment ΔL. Different implementations that have been described in Ref. [22] are depicted in Fig. 8. Most implementations [13,15–17] use the AWG network consisting of a parallel bundle of waveguides, while others have implemented a variation of the snake [14]. In this paper, we demonstrate the first implementation of an unbalanced splitter tree. The scaling properties, in terms of loss and footprint, of these three different distribution networks have been analyzed in Ref. [21].

The pixelated DOPA can leverage any of these architectures to construct the blocks of the distribution network. For the AWG architecture, it can be observed that the differential delay length ΔL used is always less than 100 μm, leading to poor resolution (>1°) along the y direction $\delta\theta_y$. Significantly increasing the differential delay length and the number of antennas for the AWG would compromise the beam quality due to the accumulation of loss and phase errors. In contrast, the snake in Ref. [14] has a remarkable $\delta\theta_y$ performance but limited x axis unambiguous steering field of view $\Delta\theta_x$ because the antennas are spaced widely apart to accommodate the "flyback" waveguides in between. In addition, it has low beam quality, but it is difficult to assess its scaling performance due to the excessively large differential delay length ΔL used in this demonstration.

It is worth noting that, when the y axis spot size FWHM_y is larger than the y axis resolution $\delta\theta_y$, the number of resolvable points becomes limited by FWHM_y, as illustrated in Figs. 9(a) and 9(b). The spot size along the y axis is entirely determined by the emission pattern of the antenna, while the separation between two scan lines is determined by the delay ΔL. Matching both values assures that there is no extra differential delay length ΔL contributing to phase errors while not adding any value in terms of the number of resolvable points.

The theoretical SLSR of any OPA is a function of the input power distribution to the antenna array. For instance, an OPA with a uniform power distribution across the aperture input has a theoretical SLSR of about 13.26 dB at an emission angle of 0° [19], while a Gaussian power distribution can have a higher SLSR depending on the truncation of the Gaussian [22]. For DOPAs, this power distribution depends on the choice of the distribution network architecture. The AWG architecture should have the highest theoretical SLSR since the input power to the aperture can have a Gaussian-like distribution due to the star coupler. The unbalanced splitter tree can have high theoretical SLSR by tuning the splitting ratio at each splitting stage to achieve a Gaussian distribution at the aperture input. The actual splitting ratios depend on the waveguide loss and number of splitting levels but generally fall between 10:90 and 90:10—values that can be well-controlled by fabrication. In contrast, constructing a well-defined Gaussian profile with a snake (II) architecture would require very small splitting ratios at the start of the array, which is difficult to control.

Apart from the power fluctuations that arise from the splitters, we also expect that fabrication variations, intrinsic to silicon photonics, will induce phase fluctuations in the waveguide delay lines. Hence, the input signal to the DOPA suffers from random fluctuations in the relative phase between the emitters resulting in degradation of the beam quality in the form of an increased level of background radiation and sometimes even prominent side lobes. In the latter case, the SLSR starts deviating from the theoretical value, which can be observed in the variation of the reported SLSRs in the works that use the same architecture [15–17]. The SLSR here becomes a function of the differential delay line length and its scaling with the number of antennas. Since the delay lengths in the pixelated DOPA do not increase to the same length as the continuous DOPA, the pixelated DOPA is therefore expected to have a better crosstalk suppression and a better SLSR, thanks to the reduced phase errors. We have also observed this in the experiments in this paper.

APPENDIX B: RESOLUTION AND BEAM DIVERGENCE ALONG THE *X* AXIS

The continuous DOPA can essentially direct a collimated beam of light to any far-field direction along a scan line. However, in terms of information content, we consider that the angular separation between two fully resolvable points along the x direction, i.e., beam divergence FWHM_x, is the separation between two distinguishable points along the x direction, i.e., angular resolution $\delta\theta_x$; see Fig. 9(c). This implies the convention that the number of far-field pixels matches the number of antennas. It follows also that there is an unnecessary coupling between the angular resolution and the beam divergence. The beam divergence specification is defined such that the Rayleigh range of the aperture is equal to the maximum projection range, so that one gets a narrow beam at maximum range. For long-range automotive LiDAR, the beam divergence specification is much smaller than the angular resolution requirement. The pixelated DOPA capitalizes on this discrepancy by disentangling the beam divergence from the angular resolution requirement [Fig. 9(d)] by subdividing the distribution network into blocks. The smaller the block size, the larger the angular resolution between the pixels.

APPENDIX C: CROSSTALK EXTRACTION METHOD

For each wavelength, the far-field images are extracted at different laser power levels, to overcome the limited dynamic range of our infrared camera. We use the image at which the maximum pixel is at the verge of saturation to locate the pixels of the main lobe and the grating lobes through a peak detection algorithm. For each laser power level, the main lobe pixel level and the 90$^{\mathrm{th}}$ percentile of the background are extracted, where examples are shown in Figs. 10(a)–10(c). The 90$^{\mathrm{th}}$ percentile is extracted by excluding the main lobe and the grating lobes pixels and then taking the 90$^{\mathrm{th}}$ percentile of all other pixels. As we know the wavelength and the pitch p_x between the antennas, we know exactly where the grating lobes are positioned relative to the main lobe.

The main lobe pixel level and the 90$^{\mathrm{th}}$ percentile pixel level are plotted versus the laser power, as shown in Fig. 10(d). The

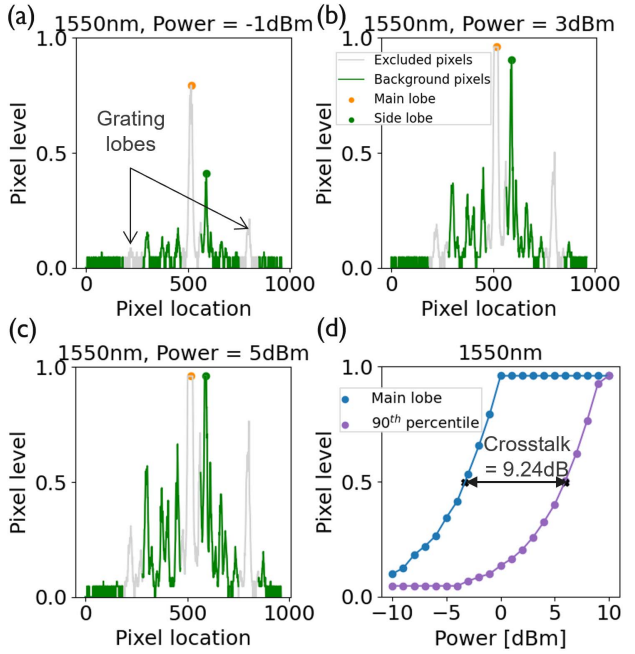

Fig. 10. Crosstalk extraction. (a)–(c) The far-field image at different input laser power levels, showing the main lobe, the grating lobes, and the background. (d) The main lobe pixel level and the 90$^{\mathrm{th}}$ percentile pixel level versus the laser power, where the crosstalk level is extracted as the difference in the laser power level at which the 90$^{\mathrm{th}}$ percentile has the same level as the main lobe.

crosstalk level is extracted by the difference in the laser power level at which the 90th percentile has the same pixel level as the main lobe. We use the difference between the laser powers at the same pixel level as sidestep possible errors due to the nonlinear response of the camera, i.e., the pixel value does not necessarily scale linearly with the impinging power.

Disclosures. The authors declare no conflicts of interest.

Data Availability. Data underlying the results presented in this paper are not publicly available at this time but may be obtained from the authors upon reasonable request.

REFERENCES

1. J. Hecht, "Lidar for self-driving cars," Opt. Photonics News **29**, 26–33 (2018).
2. B. Behroozpour, P. A. M. Sandborn, M. C. Wu, *et al.*, "Lidar system architectures and circuits," IEEE Commun. Mag. **55**, 135–142 (2017).
3. M. J. Heck, "Highly integrated optical phased arrays: photonic integrated circuits for optical beam shaping and beam steering," Nanophotonics **6**, 93–107 (2017).
4. J. Sun, E. Timurdogan, A. Yaacobi, *et al.*, "Large-scale nanophotonic phased array," Nature **493**, 195–199 (2013).
5. R. Fatemi, A. Khachaturian, and A. Hajimiri, "A nonuniform sparse 2-D large-FOV optical phased array with a low-power PWM drive," IEEE J. Solid-State Circuits **54**, 1200–1215 (2019).
6. T. Fukui, R. Tanomura, K. Komatsu, *et al.*, "Non-redundant optical phased array," Optica **8**, 1350–1358 (2021).
7. H. Qiu, Y. Liu, X. Meng, *et al.*, "Ultra-sparse aperiodic silicon optical phased array using high-performance thermo-optic phase shifter," Laser Photonics Rev. **18**, 2301177 (2024).
8. K. V. Acoleyen, W. Bogaerts, J. Jágerská, *et al.*, "Off-chip beam steering with a one-dimensional optical phased array on silicon-on-insulator," Opt. Lett. **34**, 1477–1479 (2009).
9. J. C. Hulme, J. K. Doylend, M. J. R. Heck, *et al.*, "Fully integrated hybrid silicon two dimensional beam scanner," Opt. Express **23**, 5861–5874 (2015).
10. D. N. Hutchison, J. Sun, J. K. Doylend, *et al.*, "High-resolution aliasing-free optical beam steering," Optica **3**, 887–890 (2016).
11. T. Kim, P. Bhargava, C. V. Poulton, *et al.*, "A single-chip optical phased array in a wafer-scale silicon photonics/CMOS 3D-integration platform," IEEE J. Solid-State Circuits **54**, 3061–3074 (2019).
12. Z. Zhou, W. Xu, C. Liu, *et al.*, "Butler matrix enabled multi-beam optical phased array for two-dimensional beam-steering and ranging," Photonics Res. **12**, 912–920 (2024).
13. K. Van Acoleyen, W. Bogaerts, and R. Baets, "Two-dimensional dispersive off-chip beam scanner fabricated on silicon-on-insulator," IEEE Photonics Technol. Lett. **23**, 1270–1272 (2011).
14. N. Dostart, B. Zhang, A. Khilo, *et al.*, "Serpentine optical phased arrays for scalable integrated photonic lidar beam steering," Optica **7**, 726–733 (2020).
15. P. Muñoz, D. Pastor, L. A. Bru, *et al.*, "Scalable switched slab coupler based optical phased array on silicon nitride," IEEE J. Sel. Topics Quantum Electron. **28**, 0001701 (2022).
16. L. Yu, P. Wang, P. Ma, *et al.*, "Two-dimensional beam scanning of passive optical phased array based on silicon nitride delay line," J. Lightwave Technol. **41**, 2756–2764 (2023).
17. Y. Misugi, T. Nakano, and T. Kita, "Silicon-based high-resolution and low-power-consumption two-dimensional beam scanner integrated with hybrid wavelength-tunable laser diode," Opt. Express **32**, 13746–13760 (2024).
18. Y. Yang, Y. Ma, H. Guan, *et al.*, "Phase coherence length in silicon photonic platform," Opt. Express **23**, 16890–16902 (2015).
19. C. A. Balanis, *Antenna Theory: Analysis and Design* (John Wiley & Sons, 2016).
20. I. Kim, R. J. Martins, J. Jang, *et al.*, "Nanophotonics for light detection and ranging technology," Nat. Nanotechnol. **16**, 508–524 (2021).
21. W. Bogaerts, M. Dahlem, S. Dwivedi, *et al.*, "Dispersive optical phased array circuit for high-resolution pixelated 2D far-field scanning controlled by a single wavelength variable," Proc. SPIE **11284**, 112841Z (2020).
22. W. Bogaerts, S. Dwivedi, R. Jansen, *et al.*, "A 2D pixelated optical beam scanner controlled by the laser wavelength," IEEE J. Sel. Topics Quantum Electron. **27**, 6100512 (2021).
23. R. Baets, A. Z. Subramanian, S. Clemmen, *et al.*, "Silicon photonics: silicon nitride versus silicon-on-insulator," in *2016 Optical Fiber Communications Conference and Exhibition (OFC)* (2016), pp. 1–3.
24. A. Rahim, J. Goyvaerts, B. Szelag, *et al.*, "Open-access silicon photonics platforms in Europe," IEEE J. Sel. Topics Quantum Electron. **25**, 8200818 (2019).
25. T. Kim, "Realization of integrated coherent lidar," Ph.D. Thesis (University of California, 2019).
26. L. V. Iseghem and W. Bogaerts, "Optical leaky fin waveguide for long-range optical antennas on high-index contrast photonic circuit platforms," Photonics Res. **11**, 1570–1582 (2023).
27. A. Marinins, J. Kjellman, M. Prost, *et al.*, "Bragg reflector co-integrated with SiN and a-Si on 300 mm wafers for low loss optical beamformers," in *2022 Conference on Lasers and Electro-Optics (CLEO)* (2022), paper SM4G.6.
28. W. Bogaerts, M. Kandil, and M. S. Dahlem, "Integrated optical beam scanning and FMCW ranging using multiplexed tunable lasers," in *2022 IEEE Photonics Conference (IPC)* (2022), pp. 1–2.
29. L.-R. Robichaud and S. Duval, "Short pulse mid-IR fiber lasers for advanced applications in industry and science," in *2022 Conference on Lasers and Electro-Optics (CLEO)* (2022), paper JM4E.3.
30. H. Guan, A. Novack, T. Galfsky, *et al.*, "Widely-tunable, narrow-linewidth iii-v/silicon hybrid external-cavity laser for coherent communication," Opt. Express **26**, 7920–7933 (2018).
31. J. Zhang, B. Haq, J. O'Callaghan, *et al.*, "Transfer-printing-based integration of a III-V-on-silicon distributed feedback laser," Opt. Express **26**, 8821–8830 (2018).
32. M. Kandil, M. Dahlem, and W. Bogaerts, "System trade-offs in a swept source FMCW lidar with dispersive opa beam steering," in *Smart Photonic and Optoelectronic Integrated Circuits 2024* (SPIE, 2024), pp. 102–114.
33. J. H. Song, T. D. Kongnyuy, A. Stassen, *et al.*, "Adiabatically bent waveguides on silicon nitride photonics for compact and dense footprints," IEEE Photonics Technol. Lett. **28**, 2164–2167 (2016).